Journal of Applied Physics

Properties of topological crystalline insulator $Pb_{0.5}Sn_{0.5}Te$ epitaxial films doped with bismuth

Cite as: J. Appl. Phys. **131**, 085302 (2022); https://doi.org/10.1063/5.0080329
Submitted: 30 November 2021 • Accepted: 08 February 2022 • Published Online: 25 February 2022

B. A. Kawata, C. I. Fornari, P. Kagerer, et al.

ARTICLES YOU MAY BE INTERESTED IN

DFT investigation of physical properties and electronic structure of metastable cubic CrC partially substituted with transitional metals
Journal of Applied Physics **131**, 085108 (2022); https://doi.org/10.1063/5.0077047

Dynamics of the transition resistance of Al–(Ti, Ni, Mo)–Si type contacts under conditions of non-stationary electrical loads
Journal of Applied Physics **131**, 083901 (2022); https://doi.org/10.1063/5.0084330

Shock wave diagnostics with an ultra-short optical fiber probe
Journal of Applied Physics **131**, 085903 (2022); https://doi.org/10.1063/5.0079204

© 2022 Author(s).

Journal of Applied Physics ARTICLE scitation.org/journal/jap

Properties of topological crystalline insulator $Pb_{0.5}Sn_{0.5}Te$ epitaxial films doped with bismuth

Cite as: J. Appl. Phys. **131**, 085302 (2022); doi: 10.1063/5.0080329
Submitted: 30 November 2021 · Accepted: 8 February 2022 ·
Published Online: 25 February 2022

B. A. Kawata,[1] C. I. Fornari,[2] P. Kagerer,[2] J. Heßdörfer,[2] H. Bentmann,[2] F. Reinert,[2] A. K. Okazaki,[3] P. H. O. Rappl,[1] and E. Abramof[1,a)]

AFFILIATIONS

[1]Grupo de Pesquisa e Desenvolvimento em Materiais e Plasma-GPDMP, Instituto Nacional de Pesquisas Espaciais, São José dos Campos CEP 12201-970, SP, Brazil
[2]Experimentelle Physik VII and Würzburg-Dresden Cluster of Excellence ct.qmat, Universität Würzburg, Am Hubland, 97074 Würzburg, Germany
[3]Laboratório Nacional de Nanotecnologia, Centro Nacional de Pesquisa em Energia e Materiais, Campinas CEP 13083-970, SP, Brazil

[a)]**Author to whom correspondence should be addressed:** eduardo.abramof@inpe.br

ABSTRACT

We report here on the properties of topological crystalline insulator $Pb_{0.5}Sn_{0.5}Te$ epitaxial films doped with bismuth at levels from 0% (undoped) to 0.15%. The undoped film exhibits a *p*-type character due to metal vacancies. As the doping level rises, the hole concentration reduces. At a level of 0.06%, the electrical character inverts to *n*-type and the electron density continues to increase for rising doping level up to 0.15%. This result demonstrates an effective extrinsic *n*-type doping of $Pb_{0.5}Sn_{0.5}Te$ crystal with bismuth due to substitutional Bi atoms in metal sites. High-resolution x-ray diffraction and reciprocal space mapping show that fully relaxed high-quality films are obtained. A pristine (111) film surface is revealed after removal of the Te cover layer using a method combining Ar^+ sputtering and thermal desorption. Angle-resolved photoemission spectroscopy (ARPES) data acquired at 30 K near the $\bar{\Gamma}$ point of the undoped film surface show a parabolic-like dispersion of the bulk valence band close to the Fermi level. Now, the ARPES data for a sample doped with 0.1% of Bi reveal that the chemical potential is shifted by 40 meV upwards in the direction of the conduction band. The ARPES results also indicate that there might be a discrepancy between surface and bulk chemical potential in the doped sample. This divergence suggests that Te atoms diffuse into the surface during the thermal process to desorb the protective layer, inverting the surface to *p*-type.

Published under an exclusive license by AIP Publishing. https://doi.org/10.1063/5.0080329

I. INTRODUCTION

The pseudobinary alloy lead tin telluride ($Pb_{1-x}Sn_xTe$) crystallizes in the rock salt structure. For this semiconductor compound, the band extrema occur at the L points with a direct and narrow energy gap. For pure PbTe, the material is referred to as a trivial semiconductor, where the L^{6+} state corresponds to the valence band (VB) maximum and the L^{6-} state to the conduction band (CB) minimum. As the Sn content x increases, the energy gap decreases and vanishes at a critical Sn concentration x_c. For Sn contents higher than x_c, the bands invert with the L^{6+} and L^{6-} levels now corresponding to the CB minimum and VB maximum, respectively, and the energy gap reopens and increases until the SnTe value[1,2] [Fig. S1(a) in the supplementary material]. The critical composition increases from $x_c = 0.35$ at 4 K to $x_c = 0.56$ at 300 K [see the lower panel of Fig. S1(a) in the supplementary material]. Due to its narrow gap, the $Pb_{1-x}Sn_xTe$ material finds many applications in mid-infrared (3–14 μm) photodetectors[3] and lasers.[4]

One peculiar property of $Pb_{1-x}Sn_xTe$ semiconductor compound is its electrical character control by deviation from stoichiometry. In the case of PbTe, the homogeneity range of the phase diagram in the vicinity of the stoichiometric region includes the 50 at. % line. Therefore, either *p*-type (Pb vacancies) or *n*-type (Te vacancies) samples can be obtained by incorporating excess Te or excess Pb, respectively. On the other hand, the homogeneity range of SnTe near the stoichiometric line lies in the Te-rich side, leading only to highly *p*-type material. When alloying PbTe with SnTe, the

Published under an exclusive license by AIP Publishing

single phase range is progressively shifted to the Te-rich side (p-type side). As a consequence, for Sn contents x higher than ~0.25, extrinsic doping is needed to achieve n-type samples.[5,6]

A novel topological classification of band structures was extended to include a new class of materials called topological crystalline insulators (TCIs), which present gapless metallic surface states like a Dirac cone on crystalline planes of high symmetry.[7] These topological surface states (TSS) are protected by crystal symmetry and rise due to a nontrivial band structure system. Lead tin telluride in the inverted band regime was predicted to be the first TCI material class[8] and, due to its nontrivial topology, the TSS appear with an even number of Dirac cones on high-symmetry crystal surfaces such as (001) and (111) [Fig. S1(b) in the supplementary material]. Metallic surface bands in the format of Dirac cones were experimentally observed in angle-resolved photoemission spectra (ARPES) on the (001) plane at the border of the $\bar{X}$ point along the $\bar{\Gamma}$-$\bar{X}$ linecut on SnTe[9] and $Pb_{0.6}Sn_{0.4}Te$[10] bulk crystals. ARPES spectra measured on the (111) surface of SnTe bulk crystal[11] and $Pb_{1-x}Sn_xTe$ epitaxial film[12] also revealed the Dirac cones near the $\bar{\Gamma}$ and $\bar{M}$ points. These are the first experimental evidence of a TCI. Due to the topological properties, $Pb_{1-x}Sn_xTe$ was selected as a potential candidate for use in spintronic devices.[13]

Probing TSS in the PbSnTe system by electronic transport experiments is always hampered by the large intrinsic charge carriers in the bulk. Alternatively, topological surface states have been indirectly observed by magneto-optical experiments using infrared Landau level spectroscopy in PbSnTe and PbSnSe epitaxial films.[14] In controversy, the same experiments performed on PbSnTe epilayers with compositions in the topological regime (band-inverted region) have not found any clear signature of the symmetry-protected topological surface states.[15] Moreover, the investigation of the photoelectromagnetic (PEM) effect induced by terahertz laser radiation in PbSnTe epitaxial films has revealed that it is possible to differentiate the PEM response produced by samples in trivial and nontrivial regimes.[16] Contrarily, experiments of the PEM effect induced by terahertz radiation on the related PbSnSe system have demonstrated that highly conductive surface electron states are present in both inverse and direct electron energy spectrum.[17] These results indicate that the presence and nature of the surface states in topological crystalline insulators are still an open question.

In order to study the topological properties of $Pb_{1-x}Sn_xTe$, it is desirable to have a good control on Fermi level position and carrier density. However, the intrinsic p-type character of $Pb_{1-x}Sn_xTe$ due to the native cation vacancies, which create acceptor levels in the valence band, masks the surface states and forbids the Dirac point observation by ARPES. One way to tune the Fermi level is extrinsic n-type doping to compensate and control the carrier concentration.[18] An obstacle to the Fermi level tuning in this material can be the Fermi level pinning usually observed when doping PbSnTe with other impurities like Ga, In, or Tl.[19]

In this work, we investigate the influence of bismuth doping on the properties of $Pb_{0.5}Sn_{0.5}Te$ epitaxial films. We choose the Sn content $x = 0.50$ as it is inside the inverted band region and the transition from trivial to topological insulator can also be controlled by varying the temperature from 4 to 300 K. For this purpose, we grew by molecular beam epitaxy on (111) BaF_2 a series of 2 μm-thick $Pb_{0.5}Sn_{0.5}Te$ epifilms with different bismuth doping levels. The second set of samples with identical films covered with a protective Te layer was produced for surface experiments. High-resolution x-ray diffraction and reciprocal space mapping revealed that fully relaxed high-quality films were obtained. As the doping level is increased from 0% (undoped) to 0.15%, the electrical character inverts from p- to n-type at a level of 0.06%. For all samples, the resistivity curves exhibited a metallic behavior for $T > 90$ K and a well-defined minimum around $T = 75$ K. As revealed by low-energy electron diffraction images, a pristine (111) surface is recovered after using a method consisting of Ar^+ sputtering of the contaminated upper part of the Te cover layer followed by thermal desorption of the remaining part. Scanning tunneling microscopy images, taken after the removal of the Te protective layer, showed a film surface with a few monolayer steps originated from the step flow growth mode, corroborating with *in situ* reflection high-energy electron diffraction analysis. ARPES spectrum acquired near the $\bar{\Gamma}$ point of the undoped $Pb_{0.5}Sn_{0.5}Te$ film surface at 30 K presented a parabolic-like dispersion of the bulk valence band close to the Fermi level. Now, the ARPES spectrum of the $Pb_{0.5}Sn_{0.5}Te$ sample doped with 0.1% of Bi showed that the chemical potential of the doped sample is shifted by 40 meV (half of the $Pb_{0.5}Sn_{0.5}Te$ energy gap at 30 K) upwards in the direction of the conduction band. The ARPES results indicate that there might be a discrepancy between surface and bulk chemical potential in the doped sample. This divergence suggests that Te atoms diffuse into the surface during the thermal process to desorb the protective layer, inverting the surface to p-type.

II. EXPERIMENTAL METHODS

The samples were grown by molecular beam epitaxy (MBE) using a Riber 32P MBE system. Ionic and titanium sublimation pumps together with a liquid nitrogen cryoshroud assure the ultra-high vacuum in the main chamber. The beam equivalent pressure of the molecular fluxes was measured separately by a Bayard-Alpert ion gauge. A reflection high-energy electron diffraction (RHEED) system with an electron gun of 35 keV (EK-35 from Staib Instruments Inc.) monitors the film surface *in situ* and in real time. The RHEED patterns formed on the phosphor screen can be acquired by a CCD camera and stored in a computer for further image processing.

High-resolution x-ray diffraction (HRXRD) was carried out in an X´Pert PANalytical diffractometer. The configuration consisted of a (220) Ge four-crystal monochromator positioned after the Cu x-ray tube, i.e., monochromatic and collimated Cu Kα_1 radiation in the incident beam and a Xe proportional detector (1° of acceptance angle) for the diffracted beam.

X-ray reciprocal space mapping was performed in a Bruker high-resolution x-ray diffractometer. The system is equipped with a Göbel mirror and a Ge (220) monochromator positioned after the Cu x-ray tube, providing a collimated and monochromatic Cu Kα_1 radiation. A gas discharge detector is used to monitor the intensity of the diffracted beam.

The film's thickness was measured by scanning electron microscopy with a field emission gun (SEM-FEG) using a Tescan Mira 3 at a beam voltage of 20 kV and an in-beam SE detector.

For the electrical characterization, van der Pauw geometry samples were prepared by soldering Au wires with small In pellets.

Published under an exclusive license by AIP Publishing

Resistivity and Hall effect measurements were performed at temperatures from 13 to 300 K at a low magnetic field (0.7 T) using a Hall Keithley 180A system and a He closed-cycle cryostat.

For the surface preparation, the oxidized part of the capping layers was removed inside an ultrahigh vacuum chamber using an Ar ion sputter gun operated at 1 kV with an emission current of 10 mA. The remaining part of the protective capping layers was thermally desorbed on a manipulator at 230 °C, equipped with a PID controller to stabilize the temperature, and monitored with a 30 keV RHEED system.

The scanning tunneling microscopy (STM) measurements were performed after the thermal desorption of the capping layer, with a VT STM XA from Omicron. The base pressure in the chamber was below 7.5×10^{-10} Torr, and measurements were done at room temperature. A tungsten STM tip was electrochemically etched and preliminary tested on a Au (111) surface. STM images were recorded in constant-current mode with a bias voltage of −0.5 V and a tunneling current of 100 pA.

Low-energy electron diffraction (LEED), x-ray photoelectron spectroscopy (XPS), and angle-resolved photoemission spectroscopy (ARPES) were carried out, after the thermal desorption of the protective capping layer, with a base pressure of 7.5×10^{-11} Torr. The LEED experiment was performed at room temperature using a Thermo VG Scientific device. The XPS and ARPES experiments were conducted using an Al anode x-ray gun (Al Kα, $h\nu = 1486.7$ eV) and a monochromatized He lamp (He Iα, $h\nu = 21.2$ eV), respectively. The emitted photoelectrons were detected by a Scienta SES200 analyzer with an angular resolution of 0.2°. A polycrystalline Ag sample was measured as a reference at 30 K providing a total energy experimental resolution better than 4 meV.

III. RESULTS AND DISCUSSION

A. Sample growth and structural characterization

The $Pb_{1-x}Sn_xTe$ epitaxial films were grown by MBE on BaF_2 substrates oriented in the [111] direction. Thin slices (∼1 mm) of BaF_2 substrates were cleaved along the (111) crystalline plane just before growth and fixed onto a molybdenum sample holder using eutectic Ga-In solution. The substrates were pre-heated at 150 °C for 30 min in the preparation chamber. As transferred to the main chamber, the substrates were submitted to thermal cleaning at 300 °C for 10 min to remove all possible adsorbed contaminants prior to growth.

For this experiment, we used three effusion cells charged with solid sources of PbTe, SnTe, and Bi_2Te_3. The background pressure in the main chamber was maintained at about 10^{-10} Torr during growth. The temperatures of the PbTe and SnTe cells were tuned to obtain equal beam equivalent pressures (BEPs) of 7.7×10^{-7} Torr for both cells and assure a nominal Sn content of ∼0.5 in the $Pb_{1-x}Sn_xTe$ epitaxial films. The deposition rate was found to be 0.25 nm/s at a fixed substrate temperature of 240 °C, and the growth time was chosen to obtain a film thickness of ∼2 μm. The temperature of the Bi_2Te_3 source was varied to obtain a series of $Pb_{0.5}Sn_{0.5}Te$ samples with different Bi doping levels. The nominal doping level of Bi was estimated by the following beam fluxes ratio:

$$x_{Bi} = \frac{BEP_{Bi_2Te_3}}{BEP_{SnTe} + BEP_{PbTe}}.$$

Table I summarizes the growth parameters used to obtain the set of $Pb_{0.5}Sn_{0.5}Te$ films with Bi doping levels ranging from $x_{Bi} = 0\%$ (undoped) to $x_{Bi} = 0.15\%$. We also produced a second set of samples with the same Bi-doped $Pb_{0.5}Sn_{0.5}Te$ films covered with a 100 nm-thick Te capping layer, deposited just after growth, to protect the film surface against oxidation. This sample set is intended for STM, XPS, and ARPES experiments.

To monitor the growth dynamics, RHEED pattern images were acquired along the $[\bar{1}10]$ azimuthal direction (Fig. S2 in the supplementary material). Before starting growth, the RHEED pattern of the bare BaF_2 surface shows spots positioned on the zero-order Laue semicircle, characteristic of a flat monocrystalline surface. Just after shutters opening, the RHEED pattern abruptly changes to fixed dots on the screen, indicating that the growth starts with the nucleation of islands. After about 4 min (∼60 nm), the pattern changes to extended dots lying on a semicircle, when the islands coalesce into a continuous film with monolayer steps on the surface. This step flow growth mode persists to the end.

TABLE I. Data of the Bi-doped $Pb_{0.5}Sn_{0.5}Te$ epitaxial films grown by MBE on (111) BaF_2. Fixed MBE parameters: $T_{sub} = 240$ °C, $BEP_{PbTe} = BEP_{SnTe} = 7.7 \times 10^{-7}$ Torr. Variable MBE parameters: temperature ($T_{Bi_2Te_3}$) and beam equivalent pressure ($BEP_{Bi_2Te_3}$) of Bi_2Te_3 effusion cell. Nominal Bi doping level (x_{Bi}). Carrier type and concentration (p/n), resistivity (ρ), and Hall mobility (μ) derived from electrical measurements at 13 and 300 K. The average thickness of the films is (2.1 ± 0.2) μm.

	Parameters of Bi_2Te_3			Electrical properties at 13 K				Electrical properties at 300 K		
ID	T (°C)	BEP (10^{-10} Torr)	x_{Bi}	Carrier type	ρ (10^{-4} Ω cm)	p/n (10^{18} cm^{-3})	μ (10^3 cm^2/V s)	ρ (10^{-3} Ω cm)	p/n (10^{18} cm^{-3})	μ (10^2 cm^2/V s)
19007	…	…	0.00	p	2.7	4.2	5.4	1.3	3.8	12.0
19011	355	3.0	0.02	p	2.9	3.7	5.8	1.7	2.9	13.0
19012	380	5.0	0.03	p	7.3	2.2	3.8	3.8	2.4	6.9
20000	393	9.0	0.06	p	8.2	2.9	2.6	2.7	3.2	7.3
20001	399	11.0	0.07	n	6.6	3.2	2.9	3.2	15	1.3
19010	393	16.0	0.10	n	2.8	4.4	5.1	1.6	7.2	5.2
20002	413	23.0	0.15	n	3.0	5.8	3.6	1.6	9.4	4.2

Published under an exclusive license by AIP Publishing

For the x-ray diffraction characterization, ω–2θ scans were measured around the (222) Bragg peaks for all samples. The x-ray diffraction curve of one sample (ID20001) is displayed in the graph of Fig. 1(a) and exhibits well resolved PbSnTe and BaF_2 peaks. The BaF_2 substrate peak (lattice constant $a_{BaF2} = 6.200$ Å) is used as a reference for the θ scale. Very similar ω–2θ scans were obtained for all other samples and, as expected, the Bi doping had no influence on the x-ray diffraction curves. The lattice parameter of the films was determined from the angular separation between the PbSnTe and BaF_2 peaks and its mean value was found to be (6.393 ± 0.002) Å within the series.

Assuming a linear dependence of lattice constant on alloy composition (Vegard's law), which is valid for $Pb_{1-x}Sn_xTe$ alloy,[20] the actual Sn content of each film can be determined from the measured lattice parameter a by the relation

$$x = \frac{a_{PbTe} - a}{a_{PbTe} - a_{SnTe}},$$

where a_{PbTe} and a_{SnTe} are the bulk lattice parameters of PbTe and SnTe, respectively. Using $a_{PbTe} = 6.462$ Å and $a_{SnTe} = 6.327$ Å, the average Sn content within the set of samples was determined to be $x = (0.51 \pm 0.02)$.

The full-width at half-maximum (FWHM) obtained for the $Pb_{0.5}Sn_{0.5}Te$ peak was (330 ± 30) arcsec among the samples. As disorder in any pseudobinary alloy is maximum for contents around 50%, this FWHM value found for $Pb_{0.5}Sn_{0.5}Te$ film is very reasonable when compared to 100 arcsec for PbTe[21] and 200 arcsec for SnTe.[22] In this sense, $Pb_{0.5}Sn_{0.5}Te$ films with high crystalline quality were obtained here.

To further analyze the sample structure, reciprocal space maps (RSMs) were recorded around the symmetrical (222) and asymmetrical (513) lattice points of substrate and film and are shown in Fig. 1(b). The colorbars represent the scattered intensity in cps in a logarithmic scale. On the asymmetrical (513) RSM, the $Pb_{0.5}Sn_{0.5}Te$ reciprocal lattice point lies exactly along the line that connects the points of bulk SnTe and PbTe represented by the green symbols in the map. This result demonstrates that the 2 μm-thick films are completely relaxed, exhibiting an undistorted cubic unit cell with no residual strain. Also, the center of the film peak lies in the middle of this line, as expected for a PbSnTe film with 50% of Sn content. The positions of the reciprocal lattice points corresponding to the materials fully strained to the BaF_2 substrate are represented by red symbols. To calculate the strained positions, we used the elastic constants of bulk PbTe and SnTe and a linear interpolation between these values for the $Pb_{0.5}Sn_{0.5}Te$ alloy. The broadening of the scattered intensity around the $Pb_{0.5}Sn_{0.5}Te$ reciprocal lattice point, especially visible on the (222) RSM, is mainly due to dislocations formed during the initial stage of growth to accommodate the lattice mismatch of 3% between film and substrate.

Figure 2(a) shows electron microscopy images of the samples cross section. The thickness of the $Pb_{0.5}Sn_{0.5}Te$ films within the series, obtained from these SEM-FEG images, presented an average value of (2.1 ± 0.2) μm. From this image, one can clearly observe the occurrence of gliding dislocations near to the film–substrate interface, which is consistent with the islands nucleation at the growth beginning seen in the RHEED analysis. This image shows that the dislocations density reduces significantly from the interface to the top of the film. As the x-ray beam penetrates until the substrate, the broadening of the epilayer x-ray diffraction peaks shown in Fig. 1 reflects the average over the whole film.

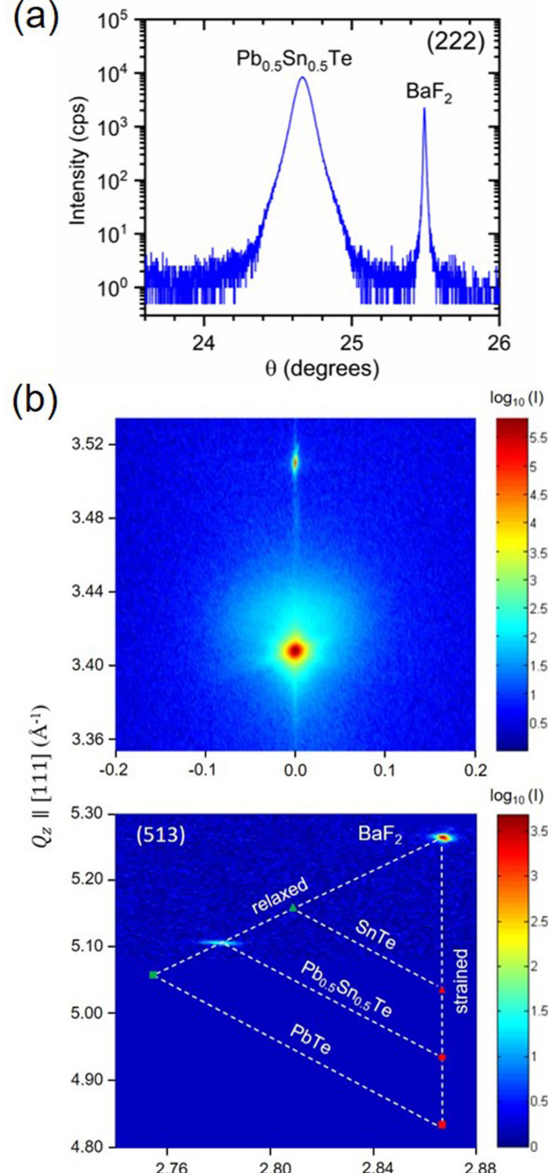

FIG. 1. X-ray diffraction analysis: (a) ω–2θ scan measured around (222) Bragg peak of a $Pb_{0.5}Sn_{0.5}Te$ / BaF_2 sample. (b) Reciprocal space maps acquired in the vicinity of the symmetrical (222) and asymmetrical (513) lattice points of BaF_2 substrate and $Pb_{0.5}Sn_{0.5}Te$ epitaxial film. The colorbars indicate the logarithm of the scattered intensity in cps.

Published under an exclusive license by AIP Publishing

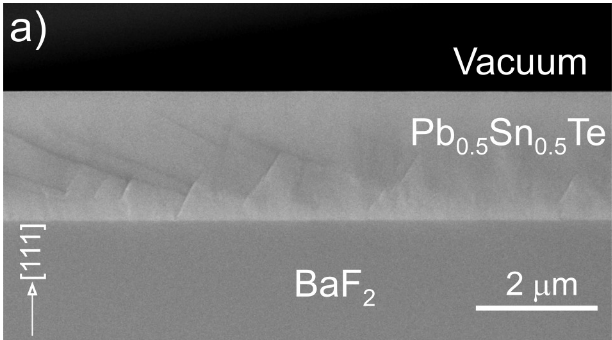

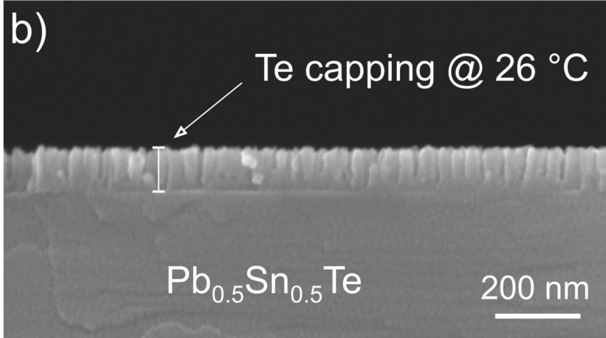

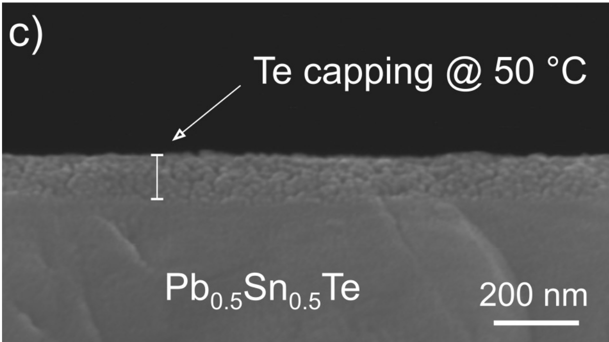

FIG. 2. Scanning electron microscopy (SEM-FEG) images: (a) Cross section of a 2 μm-thick $Pb_{0.5}Sn_{0.5}Te$ epitaxial film grown on (111) BaF_2 substrate. (b) and (c) Cross section of 100 nm-thick Te capping layers deposited on $Pb_{0.5}Sn_{0.5}Te$ films just after growth at a temperature of 26 and 50 °C, respectively.

B. Electrical characterization

The electrical properties of the Bi-doped $Pb_{0.5}Sn_{0.5}Te$ epitaxial layers were investigated by measuring resistivity and Hall effect at varying temperatures. Table I displays the carrier concentration, resistivity, and Hall mobility values at 13 and 300 K for all samples. Figure 3 shows the carrier density at 13 K as a function of the nominal Bi doping level, where a clear electrical character inversion can be observed around 0.06% of doping. As expected from the phase diagram shift to the *p*-side, the undoped $Pb_{0.5}Sn_{0.5}Te$ film exhibits a *p*-type character due to metal vacancies.

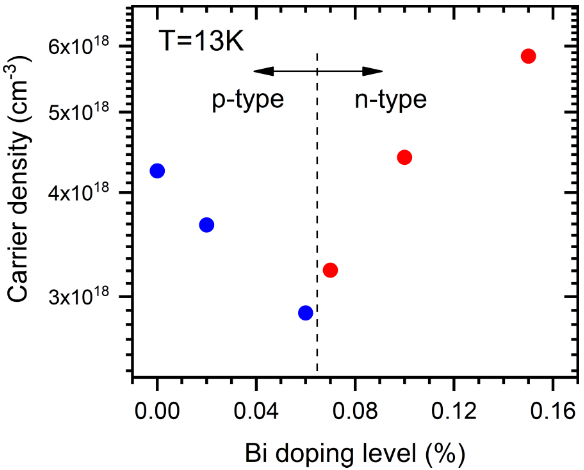

FIG. 3. Carrier concentration at 13 K as a function of nominal Bi doping level for $Pb_{0.5}Sn_{0.5}Te$ epitaxial films. A change from *p*-type to *n*-type occurs at a doping level of 0.06%.

Increasing the Bi doping level up to 0.06%, the hole concentration reduces and at a doping level of 0.07% the electrical character turns *n*-type and the electron concentration starts to increase for rising doping level up to 0.15%. This result can be explained by the electronic configuration of the elements that compose the PbSnTe alloy: [Pb] = [Xe] $4f^{14}$ $5d^{10}$ $6s^2$ $6p^2$, [Sn] = [Kr] $4f^{14}$ $5d^{10}$ $6s^2$ $6p^2$, and [Te] = [Kr] $4d^{10}$ $5s^2$ $5p^4$. These configurations lead to Pb^{2+}, Sn^{2+}, and Te^{2-} valences, respectively. For the intrinsic material, the metal ions share the valence electrons with tellurium, forming the ionic crystal. During the extrinsic doping with bismuth, the Bi atoms enter substitutionally in the metal (Pb/Sn) sites and, as bismuth has a valence 3+ with an electronic configuration [Bi] = [Xe] $4f^{14}$ $5d^{10}$ $6s^2$ $6p^3$, it shares two electrons in the ionic crystal and the exceeding electron contributes to the *n*-type doping. This result demonstrates that Bi atoms enter substitutionally in metal sites, leading to an effective extrinsic *n*-type doping of $Pb_{0.5}Sn_{0.5}Te$ crystal with bismuth.

Now, Fig. 4 exhibits the temperature dependence of carrier density, resistivity, and Hall mobility from 13 to 300 K for the Bi-doped $Pb_{0.5}Sn_{0.5}Te$ films. For the sake of clarity, we choose to plot three representative samples. The carrier density [Fig. 4(a)] can be considered to remain nearly constant in the whole temperature range independent of the electrical character or doping level, which is typical for a narrow gap semiconductor with the impurity level resonant to the band extrema or even inside the bands. The variation in carrier density is more pronounced in the temperature range from 13 to 80 K, and it turns more significant as the doping level increases. The ratio between the standard deviation and the median value within the whole temperature range is 3.2% for the undoped sample, 5.2% for the 0.06% doped film, and 14.8% for the sample doped with 0.15% of Bi. The resistivity curves [plotted in Fig. 4(b)] show an exponential increase with temperature for $T > 90$ K, demonstrating a metallic behavior for these samples. The well-defined minimum around $T = 75$ K observed in

Published under an exclusive license by AIP Publishing

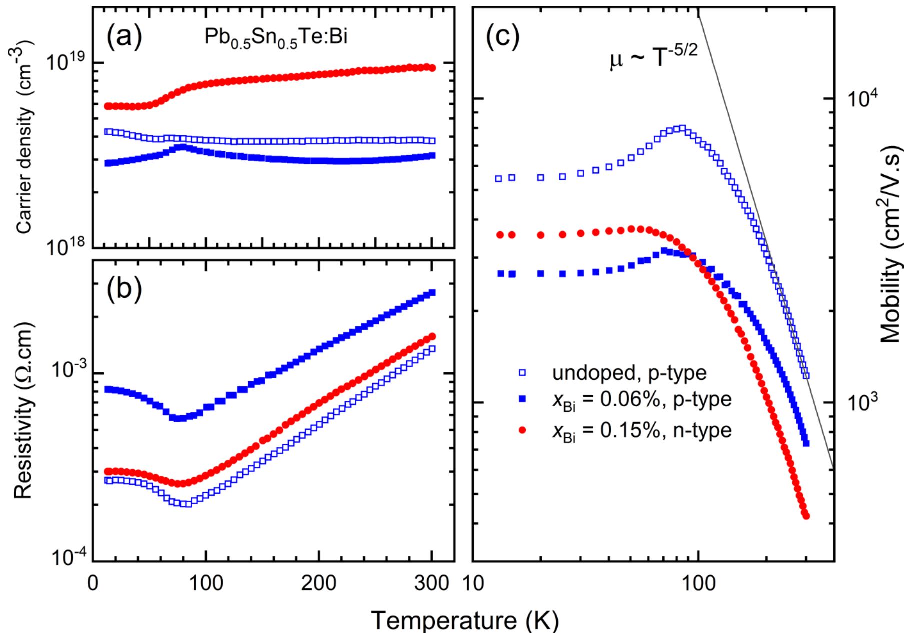

FIG. 4. Temperature dependence of (a) carrier concentration, (b) resistivity, and (c) Hall mobility of $Pb_{0.5}Sn_{0.5}Te$ films doped with bismuth.

all resistivity curves is related to the point where the band inversion occurs for the $Pb_{0.5}Sn_{0.5}Te$ alloy. At the point of band crossing, the energy gap temperature coefficient (dE_g/dT) changes sign and this influences the scattering mechanisms, leading to the anomalous behavior observed in the resistivity curves.[6,23,24] It is important to mention that the temperature (75 K) of minimum resistivity observed here differs from the value (220 K) predicted by the band inversion model[1,2] [see Fig. S1(a) in the supplementary material]. A detailed discussion on these resistivity minima observed in $Pb_{1-x}Sn_xTe$ epilayers with Sn contents inside the band inversion region ($0.35 \leq x \leq 0.70$) is found in Refs. 6 and 24. These minima in the resistivity curves of the $Pb_{0.5}Sn_{0.5}Te$ films [Fig. 4(b)] correspond to the maxima observed in the mobility curves shown in Fig. 4(c). In contrast to the carrier density temperature behavior, the change in mobility in the temperature region from 13 to 80 K turns less pronounced as the doping level rises. Additionally, the Hall mobility is limited by acoustic phonons at high temperatures according to the relation $\mu \sim T^{-5/2}$ and saturates at low temperatures due to the residual defects (mainly dislocations) present in the $Pb_{0.5}Sn_{0.5}Te$ films. These results evidence that, despite the electrical character inversion, the extrinsic doping with bismuth does not affect substantially the essential electronic properties of $Pb_{0.5}Sn_{0.5}Te$ compounds.

C. Surface analysis

1. Protective capping layer removal

As mentioned earlier, a set of Bi-doped $Pb_{0.5}Sn_{0.5}Te$ films covered with a Te capping layer was produced for the surface analysis. The capping layer is deposited just after growth in order to avoid film surface oxidation when exposing the sample to the atmosphere during storage and transfer to the surface investigation system. In a previous work,[25] we reported on a technique that combines the deposition of a protective Te capping layer on Bi_2Te_3 films just after epitaxial growth and its mechanical removal using either an adhesive tape or a glued top-post, inside an ultrahigh vacuum chamber. As Bi_2Te_3 has van der Waals coupling between its quintuple layers, resulting in the absence of dangling bonds at the surface, the Te capping is totally removed at the interface film/cap, revealing a pristine Bi_2Te_3 surface. We tried to apply this method to Te-covered PbSnTe films but the BaF_2 substrate cleaved in all attempts. This is due to the strong ionic bondings between capping and film and inside the film and also due to the weak van der Waals bonds between fluorine atoms along the [111] direction of the substrate. Therefore, we experiment here with a more complex technique to expose a pristine surface. The first step of the method consists of sputtering the surface of the capping layer using Ar^+ ions to completely remove the contaminated portion on top of the protective layer, without exposing the film. This is a crucial step to avoid contaminants to diffuse to the surface of the film during the second step, which is thermal annealing to desorb the remaining part of the capping layer.[26]

Figures 2(b) and 2(c) show the SEM-FEG images of the cross section of the $Pb_{0.5}Sn_{0.5}Te$ films covered with a Te capping layer deposited at 26 and 50 °C, respectively, just after MBE growth. Both capping layers present a thickness of 100 nm. The protective capping deposited at 26 °C [Fig. 2(b)] was found to be permeable to oxygen due to its columnar structure. Therefore, we discarded deposition of the Te layer at this low temperature. Contrarily, the Te capping layer deposited at 50 °C [Fig. 2(c)] shows a granular structure and protects the PbSnTe film surface against oxidation, as shown by XPS and LEED experiments in Fig. 5.

The XPS spectra taken as a function of Ar^+ sputtering time are plotted in Fig. 5(a). The XPS spectrum of the Te cover layer exhibits besides the $3d_{3/2}$ and $3d_{5/2}$ Te peaks and their plasmonic

Published under an exclusive license by AIP Publishing

satellites, the less intense peaks belonging to TeO located at the higher energy side near the Te 3d peaks. The inset in Fig. 5(a) plots a zoom in the vicinity of the TeO peak at 586.5 eV and shows its intensity attenuation as a function of sputtering time, indicating that the contaminated portion of the Te protective layer is completely removed after 6 h of Ar^+ sputtering. Subsequent to sputtering, LEED images of the $Pb_{0.5}Sn_{0.5}Te$ film surface were acquired at 54 eV before [Fig. 5(b)] and after [Fig. 5(c)] annealing at 230 °C during 15 min. After annealing, the LEED image presents clear spots forming the hexagonal pattern characteristic of the threefold symmetry of the (111) PbSnTe surface. The sharp and bright spots on a clear background observed in this LEED image indicate that a pristine surface is recovered after the complete removal of the protective capping layer.

2. Scanning tunneling microscopy

Figure 6(a) shows the STM image of the (111) $Pb_{0.5}Sn_{0.5}Te$ film surface after removal of the Te protective layer. The borders of the steps originated from the step flow growth mode[6] are very clear in this image in accordance with RHEED and SEM-FEG analyses described before. The depth profile along the white arrow drawn in the image of Fig. 6(a) is shown in Fig. 6(b). From this line profile, it is possible to conclude that the steps are composed of 3–4 atomic layers (MLs) of the $Pb_{0.5}Sn_{0.5}Te$ unit cell along the [111] direction ($1\,\text{ml} = a/\sqrt{3} = 0.37\,\text{nm}$ using $a = 0.6393\,\text{nm}$ for $Pb_{0.5}Sn_{0.5}Te$), represented schematically inside the graph of Fig. 6(b). This result demonstrates that the $Pb_{0.5}Sn_{0.5}Te$ surface is preserved after sputtering and annealing processes.

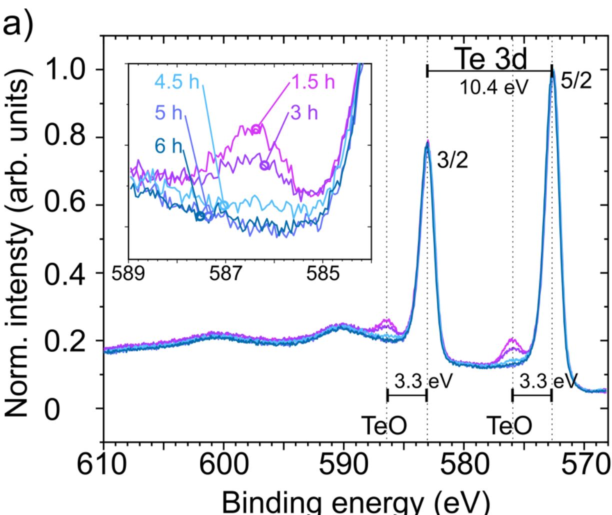

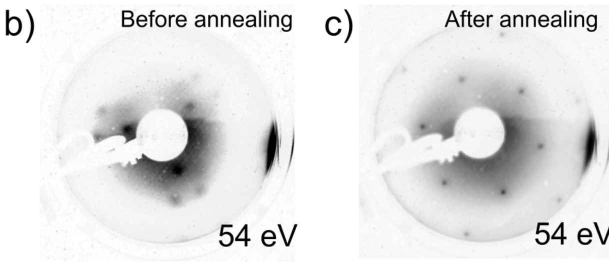

FIG. 5. (a) XPS spectra of a Te-capped $Pb_{0.5}Sn_{0.5}Te$ film taken as a function of the Ar^+ sputtering time. The inset displays a zoom near the TeO peak at 586.5 eV, demonstrating that the TeO peaks vanish after 6 h of sputtering. (b) and (c) LEED images acquired at 54 eV before and after annealing at 230 °C during 15 min, respectively, showing that the hexagonal pattern of the (111) film surface is recovered after the annealing process.

3. Angle-resolved photoemission spectroscopy

The conduction and valence bands of PbTe are mainly derived from *p*-orbitals of the cation Pb^{2+} ([Xe] $4f^{14}$ $5d^{10}$ $6s^2$ $6p^0$) and the anion Te^{2-} ([Kr] $4d^{10}$ $5s^2$ $5p^6$), respectively. On the other hand, the compound SnTe presents the conduction and valence bands derived from *p*-orbitals of Te and Sn, respectively.[9] The strong *s*–*p* coupling in SnTe is responsible for the inversion of the L^{6+} and L^{6-} bands, which remains intact in pure PbTe.[27] Figure 7 shows the ARPES results. The constant energy maps extracted at fixed binding energies from the undoped $Pb_{0.5}Sn_{0.5}Te$ sample at 30 K are presented in Fig. 7(a). The threefold symmetry from the (111) surface of PbSnTe can be clearly visualized from the Fermi level down to binding energies close to

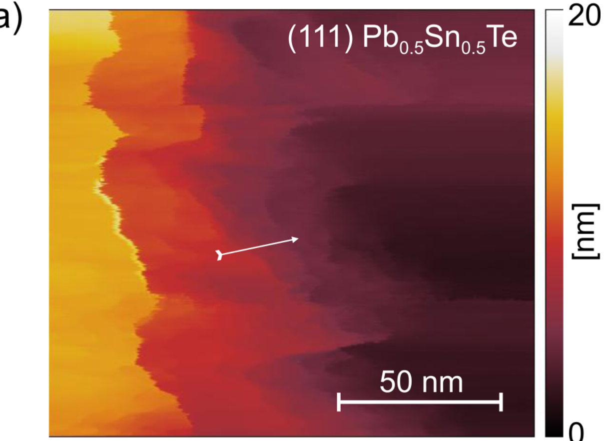

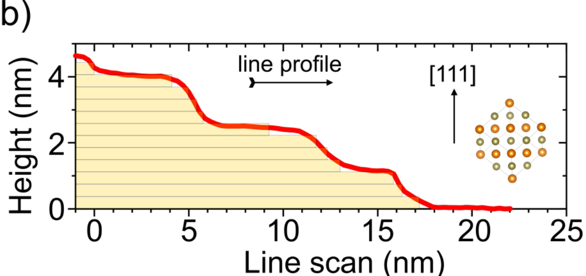

FIG. 6. (a) STM image of the (111) $Pb_{0.5}Sn_{0.5}Te$ surface after removal of the Te protective layer. (b) Depth profile along the arrow shown in (a).

Published under an exclusive license by AIP Publishing

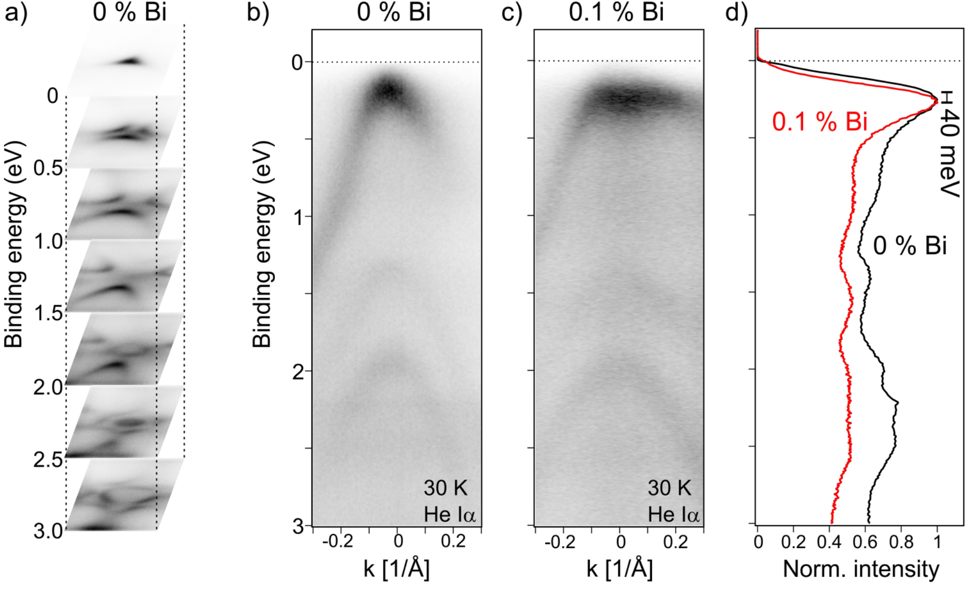

FIG. 7. Angle-resolved photoemission spectroscopy measurements on (111) $Pb_{0.5}Sn_{0.5}Te$ films at 30 K using He Iα radiation: (a) Constant energy maps extracted at different binding energies for the undoped sample. (b) and (c) ARPES spectra acquired near the $\bar{\Gamma}$ point of the undoped (0% Bi) and the 0.1% Bi-doped samples, respectively. (d) Energy distribution curves obtained by integrating the ARPES spectra of (b) and (c) from −0.3 to +0.3 $Å^{-1}$.

2 eV. The sharp dispersion and low background intensity evidence the sample quality. Figure 7(b) displays an ARPES spectrum acquired around the $\bar{\Gamma}$ point of the (111) freshly prepared surface of the undoped $Pb_{0.5}Sn_{0.5}Te$ film at 30 K. At the given photon energy (21.2 eV), the spectrum shows a parabolic-like dispersion of the bulk valence band located close to the Fermi level. As the bands are inverted at the given composition and temperature [see Fig. S1(a) in the supplementary material], the topological surface states are expected to be observed. However, due to the proximity of bulk valence band maximum to Fermi level, the topological surface states cannot be distinguished.

As discussed earlier, vacancies of the cation are thermodynamically more stable, leading to *p*-type doping, since each metal (Pb/Sn) vacancy creates two holes in the valence band.[28] In order to control the chemical potential, doping with Bi ([Xe] $4f^{14}$ $5d^{10}$ $6s^2$ $6p^3$) leads to one extra electron to the lattice since Bi takes the metal position.[19] Figure 7(c) presents the ARPES spectrum acquired in the vicinity of the $\bar{\Gamma}$ point from a $Pb_{0.5}Sn_{0.5}Te$ sample doped with 0.1% of Bi. The asymmetry of the dispersion band close to the Fermi level is due to a different azimuthal orientation with respect to the spectrum of Fig. 7(b). The chemical potential of the doped sample appears to be shifted upwards in the direction of the conduction band. It is important to mention that we can only obtain relative energy shifts from our ARPES measurements. Determination of absolute energy band positions would need photon energy dependent measurements to acquire k_z dispersions. The energy distribution curves (EDCs) for the undoped and 0.1% Bi-doped samples [shown in Fig. 7(d)] were obtained by integrating the respective ARPES spectrum in *k* from −0.3 to +0.3 $Å^{-1}$. From the comparison between both EDC curves, the chemical potential shift is found to be 40 meV upwards in the direction of the conduction band, which is approximately half of the energy gap of $Pb_{0.5}Sn_{0.5}Te$ (76 meV)[2] at 30 K. However, the bulk conduction band and the topological surface states are still not observed, showing that there might be a discrepancy between surface and bulk chemical potential. This discrepancy suggests that Te atoms diffuse into the surface of the film during the thermal process to desorb the cover layer, inverting the surface to *p*-type.[29] This *p*-type inversion is compatible with the small (40 meV) chemical potential shift observed here. Our results indicate that higher Bi doping levels and/or alternative surface preparation methods are needed to tune the surface Fermi level into the $Pb_{0.5}Sn_{0.5}Te$ conduction band, favoring the observation of the topological surface states in this material.

IV. CONCLUSIONS

We studied here the properties of Bi-doped $Pb_{0.5}Sn_{0.5}Te$ epitaxial films grown on (111) BaF_2 substrates by molecular beam epitaxy. As the doping level is raised from 0% (undoped) to 0.15%, an inversion in the electrical character from *p*- to *n*-type is observed at a level of 0.06%, demonstrating the effective extrinsic *n*-type doping with bismuth. The temperature dependent electrical results showed that, despite the electrical character inversion, the extrinsic doping with bismuth does not affect substantially the essential electronic properties of $Pb_{0.5}Sn_{0.5}Te$ compound. XPS and LEED experiments proved that a method combining Ar^+ sputtering followed by thermal desorption is capable to remove the Te protective layer and expose a pristine (111) surface of the PbSnTe film. A surface with a few monolayer steps originated from the step flow growth mode was observed by STM images recorded after the removal of the Te cover layer, in agreement with the *in situ* RHEED analysis. The ARPES spectrum acquired at 30 K around the $\bar{\Gamma}$ point of the (111) surface of the undoped $Pb_{0.5}Sn_{0.5}Te$ film exhibited the parabolic-like dispersion of the bulk valence band close to the Fermi level. A chemical potential shift of 40 meV (half

Published under an exclusive license by AIP Publishing

of the $Pb_{0.5}Sn_{0.5}Te$ energy gap at 30 K) was found in the ARPES spectrum of the 0.1% Bi-doped sample with respect to the undoped sample, which was still not sufficient to observe the bulk conduction band. The results show that there might be a divergence between surface and bulk chemical potential for the doped sample, suggesting that Te atoms diffuse into the surface during the thermal desorption process of the capping layer. Therefore, to facilitate the observation of the topological surface states in this material, higher Bi doping levels and/or alternative preparation methods are needed to tune the surface Fermi level into the $Pb_{0.5}Sn_{0.5}Te$ bulk conduction band.

SUPPLEMENTARY MATERIAL

See the supplementary material for additional information on band inversion that leads to a transition from trivial to topological regimes and on the first Brillouin zone highlighting the Dirac cones projected onto the high-symmetry crystal planes of the $Pb_{1-x}Sn_xTe$ alloy.

ACKNOWLEDGMENTS

We acknowledge the Brazilian funding agencies CAPES (Grant No. 88882.444511/2019-01) and CNPq (Grant No. 305764/2018-7) for their financial support. This work was supported by the German Research Foundation (DFG) in the framework of the Würzburg-Dresden Cluster of Excellence on Complexity and Topology in Quantum Matter ct.qmat (EXC 2147, Project No. 390858490) and SFB 1170 (Project A01). We would like to thank Dr. Martin Kamp and the Wilhelm Conrad Röntgen-Center for Complex Material Systems (RCCM) for experimental support.

AUTHOR DECLARATIONS

Conflict of Interest

The authors have no conflicts to disclose.

DATA AVAILABILITY

The data that support the findings of this study are available within the article and its supplementary material.

REFERENCES

[1] J. O. Dimmock, I. Melngailis, and A. J. Strauss, Phys. Rev. Lett. **16**, 1193–1196 (1966).
[2] G. Nimtz, B. Schlicht, and R. Dornhaus, *Narrow-Gap Semiconductors* (Springer, New York, 1983), p. 309.
[3] H. Zogg, Proc. SPIE **3629**, 52–62 (1999).
[4] M. Tacke, Philos. Trans. R. Soc., A **359**, 547–566 (2001).
[5] A. J. Strauss, Trans. Metall. Soc. AIME **242**, 354 (1968).
[6] E. Abramof, S. O. Ferreira, P. H. O. Rappl, H. Closs, and I. N. Bandeira, J. Appl. Phys. **82**, 2405–2410 (1997).
[7] L. Fu, Phys. Rev. Lett. **106**, 106802 (2011).
[8] T. H. Hsieh, H. Lin, J. Liu, W. Duan, A. Bansil, and L. Fu, Nat. Commun. **3**, 982 (2012).
[9] Y. Tanaka, Z. Ren, T. Sato, K. Nakayama, S. Souma, T. Takahashi, K. Segawa, and Y. Ando, Nat. Phys. **8**, 800 (2012).
[10] S. Y. Xu, C. Liu, N. Alidoust, M. Neupane, D. Qian, I. Belopolski, J. D. Denlinger, U. J. Wang, H. Lin, L. A. Wray, G. Landolt, B. Slomski, J. H. Dil, A. Marcinkova, E. Morosan, Q. Gibson, R. Sankar, F. C. Chou, R. J. Cava, A. Bansil, and M. Z. Hasan, Nat. Commun. **3**, 1192 (2012).
[11] Y. Tanaka, T. Shoman, K. Nakayama, S. Souma, T. Sato, T. Takahashi, M. Novak, K. Segawa, and Y. Ando, Phys. Rev. B **88**, 235126 (2013).
[12] C. Yan, J. Liu, Y. Zang, J. Wang, Z. Wang, P. Wang, Z.-D. Zhang, L. Wang, X. Ma, S. Ji, K. He, L. Fu, W. Duan, Q.-K. Xue, and X. Chen, Phys. Rev. Lett. **112**, 186801 (2014).
[13] J. Liu, T. H. Hsieh, P. Wei, W. Duan, J. Moodera, and L. Fu, Nat. Mater. **13**, 178–183 (2014).
[14] B. A. Assaf, T. Phuphachong, V. V. Volobuev, G. Bauer, G. Springholz, L.-A. de Vaulchier, and Y. Guldner, npj Quantum Mater. **2**, 26 (2017).
[15] K. K. Tikuišis, J. Wyzula, L. Ohnoutek, P. Cejpek, K. Uhlírová, M. Hakl, C. Faugeras, K. Výborný, A. Ishida, M. Veis, and M. Orlita, Phys. Rev. B **103**, 155304 (2021).
[16] A. V. Galeeva, D. A. Belov, A. S. Kazakov, A. V. Ikonnikov, A. I. Artamkin, L. I. Ryabova, V. V. Volobuev, G. Springholz, S. N. Danilov, and D. R. Khokhlov, Nanomaterials **11**, 3207 (2021).
[17] S. G. Egorova, V. I. Chernichkin, L. I. Ryabova, E. P. Skipetrov, L. V. Yashina, S. N. Danilov, S. D. Ganichev, and D. R. Khokhlov, Sci. Rep. **5**, 11540 (2015).
[18] V. V. Volobuev, P. S. Mandal, M. Galicka, O. Caha, J. Sánchez-Barriga, D. Di Sante, A. Varykhalov, A. Khiar, S. Picozzi, G. Bauer, P. Kacman, R. Buczko, O. Rader, and G. Springholz, Adv. Mater. **29**, 1604185 (2017).
[19] B. A. Volkov, L. I. Ryabova, and D. R. Khokhlov, Phys. Usp. **45**, 819–846 (2002).
[20] R. F. Bis and J. R. Dixon, J. Appl. Phys. **40**, 1918–1921 (1969).
[21] S. O. Ferreira, E. Abramof, P. H. O. Rappl, A. Y. Ueta, H. Closs, C. Boschetti, P. Motisuke, and I. N. Bandeira, J. Appl. Phys. **84**, 3650–3653 (1998).
[22] A. K. Okazaki, S. Wiedmann, S. Pezzini, M. L. Peres, P. H. O. Rappl, and E. Abramof, Phys. Rev. B **98**, 195136 (2018).
[23] S. O. Ferreira, E. Abramof, P. Motisuke, P. H. O. Rappl, H. Closs, A. Y. Ueta, C. Boschetti, and I. N. Bandeira, J. Appl. Phys. **86**, 7198–7200 (1999).
[24] J. R. Dixon and R. F. Bis, Phys. Rev. **176**, 942–949 (1968).
[25] C. I. Fornari, P. H. O. Rappl, S. L. Morelhão, T. R. F. Peixoto, H. Bentmann, F. Reinert, and E. Abramof, APL Mater. **4**, 106107 (2016).
[26] J. Dai, W. Wang, M. Brahlek, N. Koirala, M. Salehi, S. Oh, and W. Wu, Nano Res. **8**, 1222 (2015).
[27] Z.-Y. Ye, H.-X. Deng, H.-Z. Wu, S.-S. Li, S.-H. Wei, and J.-W. Luo, NPJ Comput. Mater. **1**, 15001 (2015).
[28] N. J. Parada, Phys. Rev. B **3**, 2042 (1971).
[29] A. Goyal, P. Gorai, E. S. Toberer, and V. Stevanović, NPJ Comput. Mater. **3**, 42 (2017).

Published under an exclusive license by AIP Publishing